

Space Object Characterization Using Time-Frequency Analysis of Multi-spectral Measurements from the Magdalena Ridge Observatory

Christian M. Alcala

Atmospheric and Environmental Research, Inc.

James H. Brown

Air Force Research Laboratory, Space Vehicles Directorate

1. Abstract

The interactions between the surface materials and the body dynamics complicate the characterization of space objects from their optical signatures. One method for decoupling these two effects on the observed signature is to obtain simultaneous measurements using multiple spectral filter bands. The advantage of this approach is that it provides spectral resolution between the filter bands to identify the different materials based on their optical properties as a function of wavelength and temporal resolution between samples to identify the periodic, quasi-periodic, and transient fluctuations characteristic of the object motions, including attitude control, maneuvers, and station-keeping. We have developed algorithms to extract and to analyze light curve data from unresolved resident space objects (RSO) collected at the Magdalena Ridge Observatory (MRO) using the Multi Lens Array (MLA) camera coupled to the 2.4-m telescope. The MLA camera produces 16 spectrally-filtered and temporally synchronous sub-images ranging from 414 nm to 845 nm. We have developed a filter band calibration using a set of stellar observations to remove the atmospheric refraction and absorption effects and differences in the optical paths across the different filter bands using catalogued spectrophotometric data. We apply wavelet analysis to the RSO optical signature light curves to obtain the time-frequency characteristics of the signal for each band. This information allows us to obtain information about the body motions as a function of time. We next attempt to correlate these characteristics across the different MLA filter bands to derive constraints on the types of surface materials. In this presentation, we will present results from several case studies to demonstrate the effectiveness of our approach and to provide guidance on the effectiveness of different spectral bands for space object characterization.

2. Introduction

The exponential growth of man-made objects in the near-Earth space environment over the last several decades has increased the need for accurate information about their current states and intended functions to identify and prevent possible hazards to operational satellites and space systems. For passive optical sensor systems, the quality of the observations depends on the physical properties of the object surface, the dynamics of the body, the position of the Sun, the observing conditions along the sensor line of sight to the target, and the sensitivity of the instrument. Because many of these resident space objects (RSO) are either too small or distant for the resolution of the observing sensor, they appear in optical CCD images as non-resolved point-like blobs of light intensity. In this paper, we will concentrate on analyzing non-resolved optical signatures obtained by passive sensors.

The temporal variations in the optical signatures of these objects as they move through the sensor field-of-view represent a complex interaction between the surface materials and changes in the attitude of the body. The general strategy for decoupling these interactions would include simultaneous measurements of a continuum spectrum over the region of interest for a long enough period with a fine enough resolution to capture all of the relevant dynamical timescales. The reason for this approach is that at any given instance in time, a particular sensor will measure the combination of reflections for all of the sources on the surface of the body. These individual reflections will depend on the solar phase angle between the sensor, the target, and the Sun and on the reflection properties of the materials in their different regions and their composition across the body. The reflection properties of the material are typically specified by the bidirectional reflectance distribution function (BRDF) and can depend strongly on the wavelength of the observed light. As the view of the object within the sensor varies either through attitude changes caused by spinning or tumbling motions of the object or as the geometry between the sensor and the object changes because of relative motion between the two, a new combination of material regions rotates into the sensor field-of-view, causing a variation in the observed intensity. In fact, these diverse collections of materials that form the RSO

are what actually reveal the body dynamics. Therefore, by analyzing simultaneous optical signature time series data from a given set of spectral bands, we can filter the data based on timescale features which correlate across the bands to obtain information about the attitude dynamics of the body. The residual data remaining after this filtering process will contain information about the spectral properties of the different surface materials on the object. The amount and the quality of the extracted information will depend on the extent and the resolution of the data in both the frequency and temporal domains.

3. Image Data Analysis and Non-resolved Light Curve Extraction

For the current paper, we will present results from our time-frequency analysis of the intensity light curve data obtained from the observations using the 2.4-m optical telescope together with the Multi Lens Array (MLA). P. Dao [1] provides a more detailed description of the Magdalena Ridge Observatory (MRO) telescope, the MLA, and the AFRL/SOST measurement campaign conducted during the period of 21-27 September, 2007. This instrument provides us with simultaneous measurements of a given space object in sixteen spectral filter bands. Table 1 specifies the properties of the MLA filter bands.

Table 1. MLA Optical Filter Band Specification

Band #	Wavelength	Band #	Wavelength	Band #	Wavelength	Band #	Wavelength
1	414-447 nm	5	522-563 nm	9	603-644 nm	13	726-767 nm
2	431-467 nm	6	531-569 nm	10	611-649 nm	14	743-784 nm
3	459-495 nm	7	569-609 nm	11	637-675 nm	15	780-814 nm
4	482-518 nm	8	594-636 nm	12	711-748 nm	16	808-845 nm

We have focused our efforts on the extraction and analysis of unresolved optical signatures in the data images, including both stellar and RSO observations. Each data image frame consists of 16 square sub-images, one for each filter band, in a 4x4 grid, with an additional two rectangular dark bands on the sides of the 640 x 420 pixel images. Although the original data collection applied an automatic noise estimation and removal algorithm before storage, the residual noise fluctuations can still obscure the optical signatures of dim objects. Therefore, we have estimated the variance of the noise residual using the dark side bands and compare this result with the noise estimation from the set of image amplitudes within the sixteen band data collection region of the image.

We have developed techniques to extract the light intensity curves for each band using the distribution, magnitude, and location of the optical signature. The extraction algorithm first identifies the optical signature of objects within the image using a shape analysis to correlate peak intensity values with the amplitudes of their neighboring pixels. This analysis eliminates most noise fluctuations and measurement artifacts such as cosmic ray hits, hot pixels, and system glitches and successfully detects the objects in moderate to high signal-to-noise ratio filter band observations. The algorithm uses the results of this correlation analysis to determine the full areal extent of the central peak in the optical signature intensity distribution and to calculate the centroid location and orthogonal widths of the signature. For simplicity and computational efficiency, the algorithm currently assumes the intensity distribution approximates single-peaked function rather than a more typically optical transfer function such as a sinc function and ignores the additional, albeit significantly lower, power in the fringes of the distribution. The algorithm uses this technique to process all of the image frames within a given data file.

The signature extraction algorithm next attempts to refine the optical signature estimation for the low to moderate signal-to-noise ratio filter band observations by processing the image data frames a second time using the information from the successfully extracted optical signatures. The algorithm accomplishes this task by correlating the position of the object across the filter bands for each given image frame and by tracking the object position and characteristics (area, widths, and amplitudes) from frame to frame. This approach provides us with quality control metrics for determining the effectiveness of our extraction algorithm and its robustness in the presence of multiple objects simultaneously within the image frame. We can also include the optical signature centroid position information into the estimation and removal of the effects of instrument jitter and vibration using correlation analysis with the total intensity flux variations. Fig. 1 shows an example of the results of our signature extraction algorithm for the case of stellar and RSO observations. The top panels in the Fig. show the total intensity flux for

the objects as a function of the frame time with the stellar case on the left and the RSO case on the right. The lower panels show the centroid location in the x-direction of the image for comparison.

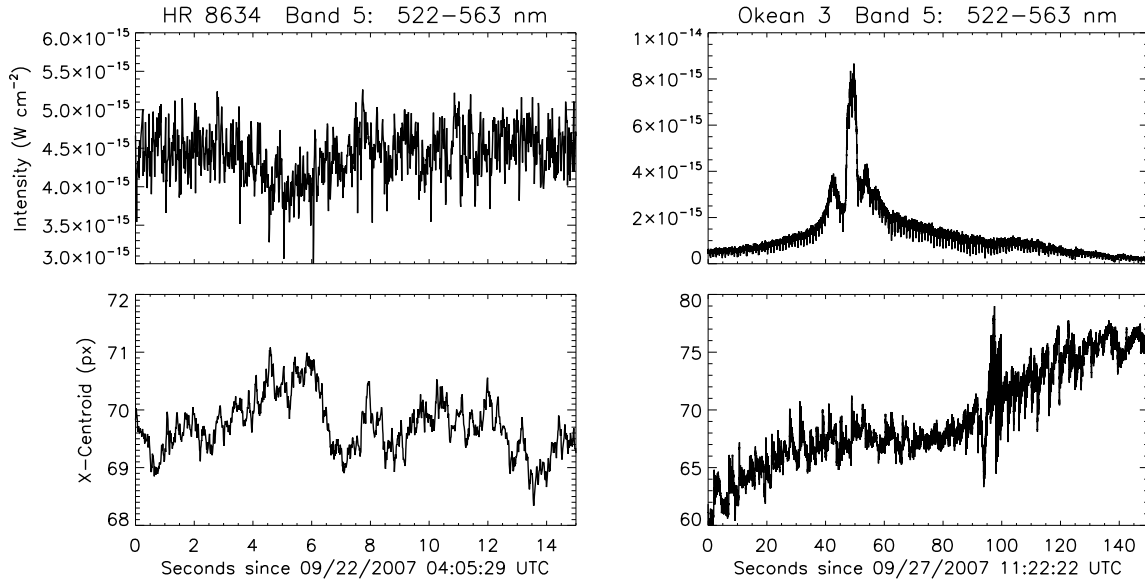


Fig. 1. Total light intensity and centroid position for stellar and RSO observations.

Although the MLA instrument generates simultaneous observations in all sixteen filter bands for each frame, the relative intensity magnitude of objects are different for each band because of differences in the optical path. We have used the stellar observations during the experiment to determine both the relative calibration between the MLA filter bands and the absolute calibration from digital counts to actual intensity flux values in units of W cm^{-2} . We have obtained the in-band calibration coefficient for each of the filter bands by comparing observed digital counts with the spectral irradiance predicted using data from a set of spectrophotometric standard stars [2,3] listed in Table 2. The calibration analysis begins with the published high wave number resolution spectral irradiance data at the top of the atmosphere and next calculates the atmospheric absorption using the ASTM G173-03 Reference Solar Spectral Irradiance model to determine the atmospheric transmission spectrum. The analysis computes the total flux for each of the sixteen MLA spectral bands by assuming the spectral window is rectangular over the wavelength range from Table 1. Fig. 2 displays the filter band calibration coefficient spectrum across the sixteen filter bands.

Table 2. Spectrophotometric standard stars used in MRO calibration analysis.

Star Designation	Proper Name	RA (J2000)	Dec (J2000)	Vmag
HR 8634	Zeta Pegasi	22:41:27	10.8314	3.4
HR 337	Mirach	1:09:43	36.6206	2.06
HR 153	Zeta Casiopeiae	0:36:58	53.8969	3.66
HR 718	Xi 2 Ceti	2:28:09	8.4601	4.28
HR 9087	29 Piscium	0:01:49	-3.0275	5.12
HR 1457	Aldabaran	4:35:55	16.5093	0.85
SAO 37734	Almach	2:03:53	42.3297	2.26
HR 7596	58 Aquilae	19:54:44	0.2734	5.62
HR 1544	Pi 2 Orionis	4:50:36	8.9002	4.36

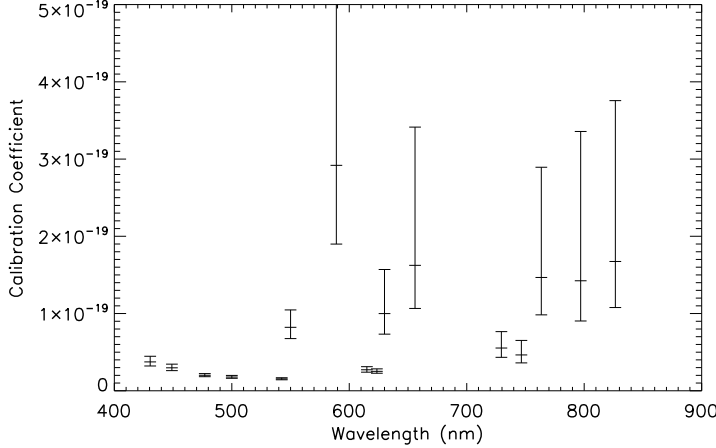


Fig. 2. MLA filter band calibration coefficients determined from MRO stellar observations.

Fig. 2 shows that the variance in the calibration coefficient values is quite large for several of the MLA filter bands. P. Dao [1] describes some of the reasons for this increases variance. The consequence of this variance is that we will not be able to use all of the spectral channels in our analysis because of low signal power and poor data quality.

4. Time-Frequency Analysis of MRO Intensity Light Curves

For a given set of light intensity time series measured from an object over a set of spectral filter bands, the entire dataset represents the contributions from a component determined by the relative motions between the sensor and the target and a component determined by the spectral properties of the composition of object surface materials visible within the sensor field-of-view. For simultaneous observations in different filter bands, we can categorize these two contributions as the sum of a component whose temporal features have a high degree of correlation across the bands and one where a low degree of correlation leads to a time-dependent set of wavelength spectra characterizing the material properties. In this paper, we will attempt to use time-frequency analysis, and in particular the wavelet transform, to identify and to estimate this motion component of the observed RSO data.

An individual RSO can manifest a wide variety of motion over its lifetime. These motions can include spinning, tumbling, orbital maneuvering, repositioning events, instrument deployment/alignment, and environmental/solar interactions. While some of these motions may have stationary oscillatory characteristics, many will vary significantly with time or show transient signatures. The time-dependent and/or transient nature of these motion signatures requires use a time-frequency analysis techniques adapted to characteristics of the temporal features. To achieve this goal, we have implemented an algorithm based on wavelet analysis. In the next two subsections, we will discuss the applicability of wavelet analysis and our use of the technique to extract the motion signatures from the intensity light curve data.

4.1. Theory of Wavelet Analysis

Because we require analysis methods capable of determining the local frequency content of the signal, we have chosen to use the wavelet transform to achieve this goal. The wavelet transform was originally developed as a method to detect thin layers of oil and gas from seismic traces [Goupillaud *et al.*, 1984] and has successfully been applied to many different fields [Foufoula-Georgiou and Kumar, 1994]. Unlike the standard Fourier transform which provides the frequency content, but no localization information, the wavelet transform divides the data into different frequency components and studies each component with a resolution matched to its scale [Daubechies, 1992]. This property means that the transform uses long time windows to analyze low-frequency components and short time windows to analyze high-frequency components. The analyzing wavelets $\psi_{a,b}$ are created by dilations a and translations b from a mother wavelet ψ as

$$\psi_{a,b}(x) = \frac{1}{\sqrt{a}} \psi\left(\frac{x-b}{a}\right)$$

The dilation scale size a is inversely proportional to the frequency. Wavelet functions are not arbitrary and must meet a set of requirements. The function must be well-localized in the time domain with a finite energy. In addition, the admissibility condition requires that the wavelet function has a zero mean value [Mallat, 1998], allowing it to function as a bandpass filter.

Although there are several types of wavelet transforms, we have restricted our analysis during this effort to the continuous wavelet transform (CWT). The CWT is the inner product of the signal $s(x)$ with the analyzing wavelets as a function of scale and time

$$S(b, a) = \int_{-\infty}^{\infty} \overline{\psi_{a,b}(x)} s(x) dx$$

Therefore, the CWT maps the 1-D signal into a 2-D parameter space of time and frequency. The magnitude of this linear map is commonly referred to as the wavelet scalogram. For analysis of sampled data sets, we have implemented a discretized version of the convolution integral using fast Fourier transforms. Similar to the Fourier transform, the CWT provides a complete and invertible representation of the signal [Mallat, 1998].

For the current analysis effort, we implemented our time-frequency analysis technique using the Morlet wavelet. This wavelet is essentially a plane wave modulated by a Gaussian window

$$\psi_M = e^{i\omega_0 t} e^{-\frac{1}{2}t^2} + c(t).$$

Although the correction term $c(t)$ must be added to satisfy the admissibility condition, in practice it is negligible for values of $\omega_0 > 5$. We show an example of the Morlet wavelet from both the time and frequency domains in Fig. 3. Because this function is complex, it is able to measure the magnitude and phase of the signal. Panel b) of Fig. 3 clearly shows the bandpass filter nature of the wavelet in the frequency-domain representation.

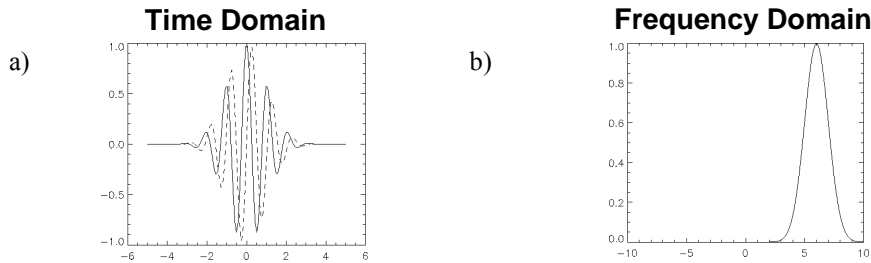


Fig. 3. Morlet wavelet example in both a) time domain and b) frequency domain. The time-domain representation shows both the real part (solid line) and the imaginary part (dashed line) of the wavelet function.

In addition to the useful filtering properties of the Morlet wavelet, it also allows for a more intuitive understanding of the analysis results than many other wavelet functions because of its similarity to the Fourier bases functions used with a Gabor window. However, the wavelet transform differs from the windowed Fourier transform in that the width of the analysis window is not fixed to a set size but varies as the scale of the analyzing wavelet changes. The most obvious similarity is that each of these wavelets appears as a little monochromatic wave, as the name implies. Therefore, we can interpret large amplitude coefficients in the wavelet scalogram as the locations where a particular wavelike feature occurs. Also because of its similarity to the Fourier bases functions, the shape of the localized spectra in the wavelet scalogram can be interpreted in terms of Fourier analysis, such as the theory developed to analyze turbulent signals.

4.2. Application of Wavelet Analysis to Intensity Light Curves

In Fig. 4, we present an example of wavelet analysis applied to two of the sixteen MLA spectral filter band time series of the light intensity. During this particular example, the MRO telescope tracked the Okean-3 satellite and recorded observations at a data rate of 80 image frames per second. The top two panels in Fig. 4 display the

intensity light curves measured in band 3 ($\lambda_c = 477$ nm) and band 13 ($\lambda_c = 746$ nm). In particular, these are two of the bands with the highest signal-to-noise ratios for this period. The total time series covers 150 seconds. In the lower two panels, we display the corresponding wavelet scalogram. In this plot, the x-axis represents the total number of elapsed seconds since the start of the time series and corresponds with the light curve intensity plots above. The y-axis displays the set of wavelet periods and represents the set of temporal frequencies covered by the analysis. The color scale represents the magnitude of the wavelet scalogram coefficients for a given time and period. We can see from this example that the wavelet coefficients reach their peak amplitudes over the period of time where the intensity light curve maximizes in power. By examining the wavelet coefficients, we can determine that both of the two intensity light curves have strong location oscillation with a period of 6-7 seconds at an elapsed time value of about 50 seconds. We can also see a second oscillation centered on this same time period with a wavelet period of ~ 50 seconds. The advantage of the wavelet transform is that it allows us to identify and to characterize the temporal features within the signal.

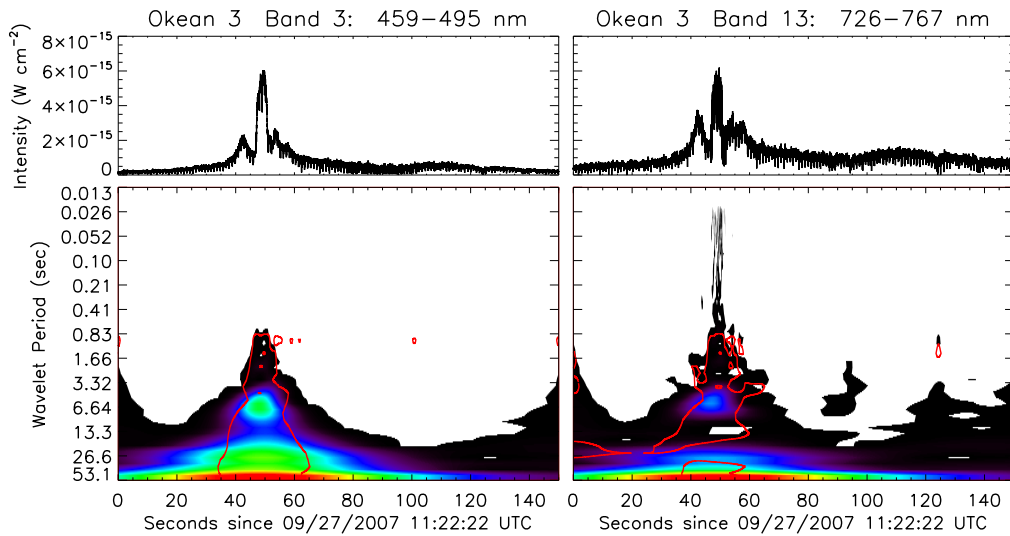


Fig. 4. Morlet wavelet analysis of the total light intensity observed in MLA band 3 and band 13 from the Okean-3 Satellite.

In order to extract useful information from the wavelet analysis, we need a method for identifying the scalogram coefficients corresponding to the temporal features of the most interest. We also require a method for determining and quantifying the significance of a particular feature detected with the wavelet analysis. The first step in this process is, of course, to match the wavelet basis function to the desired types of phenomena. We have briefly discussed our choice of the Morlet wavelet for the detection of motion signatures in the previous section. In order to distinguish between the presence of real temporal features and spurious noise peaks, we have implemented the statistical significance testing for the wavelet analysis derived by Torrance and Compo [8]. This test uses the global wavelet spectrum to determine the probability of a noise fluctuation exceeding a given amplitude threshold. For our analysis, we have set this threshold value to correspond to a 90% confidence interval.

Fig. 4 displays this confidence interval as a red contour line overlay on the wavelet scalogram. We have neglected plotting the contour lines for the features with wavelet periods less than 0.5 seconds because this region is dominated by sharp transients caused by the tracking motion of the MRO telescope. Ideally, we should apply a method to identify and remove these motion transients by correlating the optical signature centroid position with the total integrated light intensity. However, we have not done this task for the current analysis and will ignore the effects of these transients on the partitioning of the filter band signal between the motion and the materials components. Comparison of the wavelet scalogram results of the two filter band signals in Fig. 4 reveals that the most significant temporal features in the signal occur in the region centered on an elapsed time of 50 seconds and cover a range of wavelet periods from ~ 0.8 -50 seconds. A visual examination of the intensity signal indicates that these results agree with the expected results. However, the advantage of the wavelet analysis is that we now have a

quantitative range of values for the motion signatures in both time and frequency, which can be used to automate the process of feature detection and characterization.

5. Extraction of RSO Motion Signatures

Now that we have developed our analysis tools, we can begin to apply them to the task of partitioning the RSO intensity signal between the motion and materials components. Because the wavelet transform provides an invertible representation of the signal for the proper set of bases functions, we can obtain a reconstruction of the data by performing a summation over the wavelet coefficients [6]. We can exploit this property to develop a wavelet-based filtering algorithm using a partial set of wavelet coefficients to reconstruct a signal corresponding only to a set of temporal features of interest. Subtracting this filtered signal from the original signal will result in a decomposition of the data into two components composed of different types of temporal features. We should point out that this type of wavelet filtering differs fundamentally from Fourier filtering in that the amplitude of the transform coefficients are used rather than their scale sizes. Therefore, the resulting signal can contain both high- and low-frequency components.

For the current analysis, we will begin with the initial assumption that the most significant wavelet components correspond to the motion signature in the current data set. A partial justification for this assumption comes from an examination of the wavelet scalogram plots in Fig. 4 showing the analysis of the intensity light curves from MLA filter bands 3 and 13. We can see that the significance contours on both of these plots correlate quite well in terms of both the elapsed time location and the range and wavelet periods. Although not shown here, this pattern repeats in all of the MLA filter bands where the signal-to-noise ratio is high. A more complete analysis would involve a full correlation analysis across all of the useable MLA filter bands. However, in the current study, we wish to demonstrate the feasibility of our analysis technique to the partitioning problem.

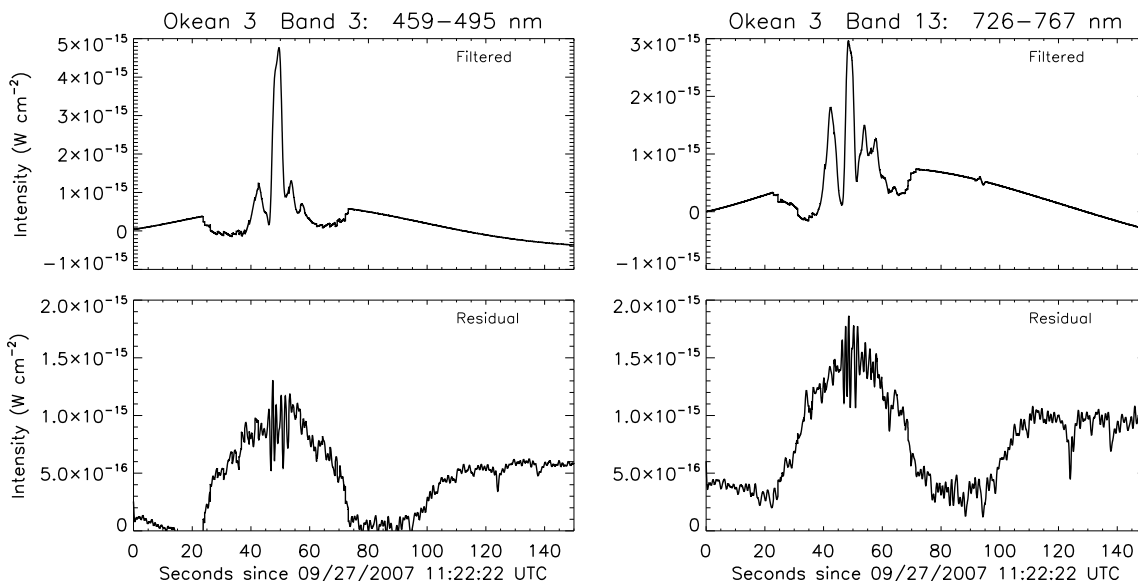


Fig. 5. Results of wavelet-based filtering algorithm to partition intensity light curves between motion and materials components.

Fig. 5 displays the results of our wavelet-based filtering algorithm for the light intensity observations of the Okean-3 satellite from MLA filter bands 3 and 13. The top two panels show the wavelet-filtered signal produced by the reconstruction from the most significant wavelet coefficients, neglecting the contributions due to tracking motion transients. We can see that the extracted motion features signals show similar characteristics in both of the two filter bands. The lower two panels display the residual signal obtained after subtraction of the wavelet-filtered signal from the original intensity time series. We have also removed a noise signal from the residual signal created from the high-frequency components of the wavelet transform using a scale threshold based on the global wavelet spectrum. Based on our assumption about the wavelet coefficients used for the filtering of the motion components,

this residual signal should contain information about the surface materials on the object. To provide additional support for this claim, we have plotted the ratio of these two residual intensity light curves in Fig. 6 in order to prove that the wavelength spectra of the RSO varies as a function of time. Before computing the spectral ratio, we have smoothed the residual intensity time series using a 6-second time window for visualization purposes. Fig. 6 shows how the different spectral components vary in magnitude relative to each other as different regions of the object body rotate into the view of the sensor. Matching the results from a full set of spectral bands with measured databases of material optical properties would allow retrieval of information about the types and compositions of the surface materials.

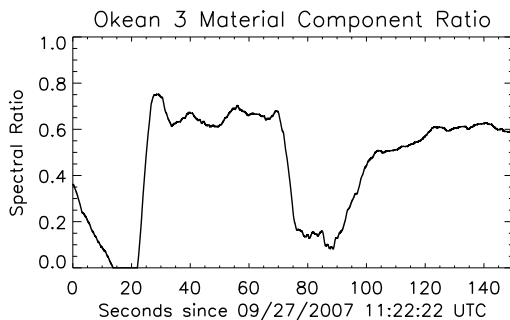


Fig. 6. Intensity ratio between the materials components extracted from MLA bands 3 and 13 after wavelet filtering.

We have also applied this wavelet analysis technique to MLA observations from the ADEOS satellite. We present the results of the wavelet filtering for the spectral bands 3 and 13 in Fig. 7. The top two panels display the light intensity data collected in the two spectral bands during the tracking of this object. The optical signatures are dominated by a sudden flash of intensity at about 150 seconds into the time series. The intensity light curves exhibit more difference between the two spectral bands than the Okean-3 data contained. The middle two panels give the wavelet-filtered results corresponding to the motion features in the signal and the lower two panel display the residual signal containing the surface materials features. In the residual signals, two peak regions appear in both of the filter bands with the first centered at an elapsed time of 150 seconds and the second centered at 300 seconds. Fig. 8 displays the spectral ratio computed from the residual intensity curves for the two bands. We have once again applied a 6-second smoothing window to the data for visualization purposes. The spectral ratio curve also contains these two peak regions, indicating that different regions of the body have moved into the sensor view during these times.

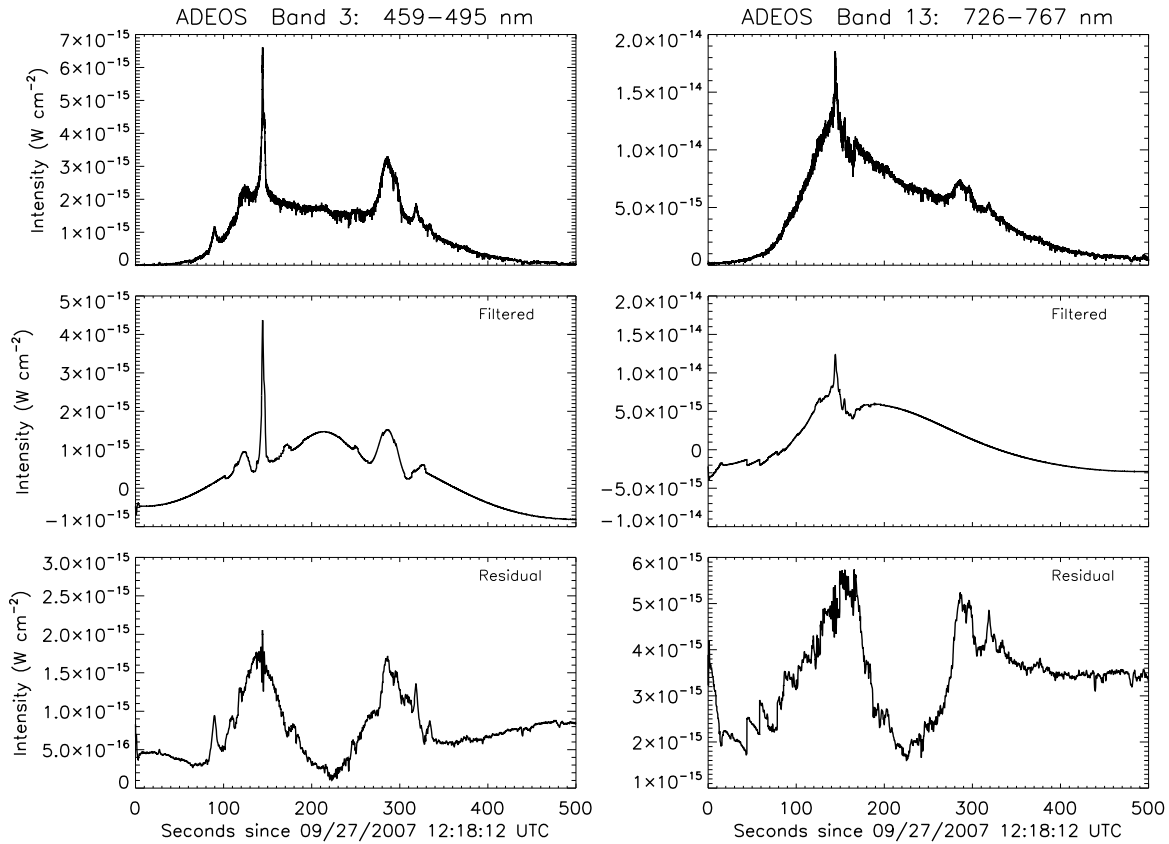


Fig. 7. Wavelet filtering results from MLA band 3 and 13 observations of the ADEOS satellite.

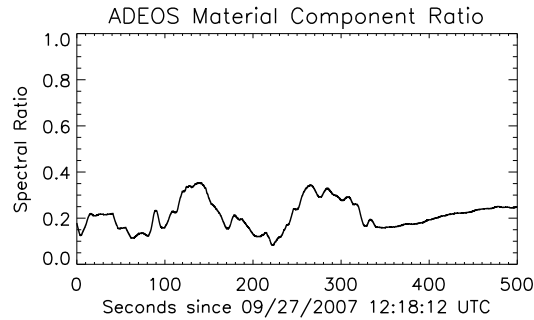


Fig. 8. Spectral ratio of the residual intensity light curves from MLA bands 3 and 13 for observations of the ADEOS satellite.

6. Conclusions

The goal of this current analysis is to study the time-frequency characteristics of the light intensity signal observed from an unresolved RSO over multiple spectral bands in an attempt to decouple the contributions from the motions of the body and the illuminated surface materials. We have outlined and presented initial results from a technique using wavelet analysis to identify the motion signature in the intensity light curve and to filter this component of the signal. We show how to complete the decomposition of the data by removing this contribution from the observed intensity to obtain an intensity signal dominated by the behavior of the surface material properties. We have examined the feasibility of this technique using RSO data collected using the sixteen spectral band MLA instrument on the MRO 2.4-m telescope. The technique can provide information about the spectrum of the materials as a

function of time. We have presented our results from this technique as the ratio of the intensities from the two residual components in filter bands centered at 477 nm and 746 nm.

7. Acknowledgments

We would like to acknowledge Eileen V. Ryan and William Ryan from the Magdalena Ridge Observatory for gathering the data using in this paper. This work was supported by AFRL through contract FA8718-05-C-0088.

8. References

1. Dao, P. D., P. J. McNicholl, J. H. Brown, J. E. Crowley, M. J. Kendra, P. N. Crabtree, A. V. Dentamaro, E. V. Ryan, and W. Ryan, Space Object Characterization with 16-Visible-Band Measurements at Magdalena Ridge Observatory, Advanced Maui Optical and Space Surveillance Technologies Conference, Maui, Hawaii, 2008.
2. Hamuy, M., A.R. Walker, N.B. Suntzeff, P. Gigoux, S.R. Heathcote, and M.M. Phillips, Southern Spectrophotometric Standards. I., *Publications of the Astronomical Society of the Pacific*, 104, 533-552, 1992.
3. Hamuy, M., N.B. Suntzeff, S.R. Heathcote, A.R. Walker, P. Gigoux, and M.M. Phillips, Southern Spectrophotometric Standards. II., *Publications of the Astronomical Society of the Pacific*, 106, 566-589, 1994.
4. Goupillaud, P., A. Grossmann, and J. Morlet, Cycle-octave and related transforms in seismic signal analysis, *Geoexploration*, vol. 23, 85-102, 1984.
5. Fofoula-Georgiou, E. and P. Kumar, *Wavelets in Geophysics*, Academic Press, 1994.
6. Daubechies, I., *Ten Lectures on Wavelets*, SIAM, 1992.
7. Mallat, S., *Wavelet Tour of Signal Processing*, Academic Press, 1998.
8. Torrence C. and G.P. Compo, A Practical Guide to Wavelet Analysis, *Bulletin of the American Meteorological Society*, vol. 79, 1, 61-78, 1998.